

Sea-Land-Cloud Segmentation in Satellite Hyperspectral Imagery by Deep Learning

Jon Alvarez Justo^a, Joseph L. Garrett^a, Mariana-Iuliana Georgescu^b, Jesus Gonzalez-Llorente^c,
Radu Tudor Ionescu^b, Tor Arne Johansen^a

^a*Dept. Engineering Cybernetics, Norwegian University of Science and Technology, Trondheim, Norway*

^b*Dept. of Computer Science, University of Bucharest, Romania*

^c*Independent Consultant, Montreal, Canada*

Abstract

Satellites are increasingly adopting on-board AI for enhanced autonomy through in-orbit inference. In this context, the use of deep learning (DL) techniques for segmentation in hyperspectral (HS) satellite imagery offers advantages for remote sensing applications, and therefore, we train 16 different models, whose codes are made available through our study, which we consider to be relevant for on-board multi-class segmentation of HS imagery, focusing on classifying oceanic (sea), terrestrial (land), and cloud formations. We employ the HYPSONO-1 mission as an illustrative case for sea-land-cloud segmentation, and to demonstrate the utility of the segments, we introduce a novel sea-land-cloud ranking application scenario. We consider how to prioritize HS image downlink based on sea, land, and cloud coverage levels from the segmented images. We comparatively evaluate the models for future in-orbit deployment, considering performance, parameter count, and inference time. The models include both shallow and deep models, and after we propose four new DL models, we demonstrate that segmenting single spectral signatures (1D) outperforms 3D data processing comprising both spectral (1D) and spatial (2D) contexts. We conclude that our lightweight DL model, called 1D-Justo-LiuNet, consistently surpasses state-of-the-art models for sea-land-cloud segmentation, such as U-Net and its variations, in terms of performance (0.93 accuracy) and parameter count (4,563). However, the 1D models present longer inference time (15s) in the tested processing architecture, which seems to be a suboptimal architecture for this purpose. Finally, after demonstrating that in-orbit segmentation should occur post L1b radiance calibration rather than on raw data, we also show that reducing spectral channels down to 3 lowers models' parameter counts and inference time, at the cost of weaker segmentation performance.

Keywords: Remote Sensing, Satellite Imagery, Hyperspectral Imaging, Deep Learning, Segmentation

1. Introduction

ARTIFICIAL INTELLIGENCE (AI) has seen a growing utilization aboard satellite platforms for remote sensing, benefiting Earth observation missions equipped with various technologies from conventional RGB to both Multispectral Imaging (MSI) and Hyperspectral Imaging (HSI). The importance of monitoring the Earth's environment with HSI technology is emphasized by the use of hyperspectral (HS) imagers in numerous contemporary satellite missions, e.g., ESA/Phi-Sat-1 [1], ASI/PRISMA [2, 3], DLR/EnMAP [4], and NTNU/HYPSONO-1 [5]. The importance of HS imagers on satellites is further highlighted by upcoming missions, e.g., ESA/CHIME [6, 7], NASA/PACE, GLIMR and SBG [8], ASI/PRISMA Second Gen [9], as well as

NTNU/HYPSONO-2 and NTNU/HYPSONO-3 [10]. HS missions offer great potential due to their detailed spectral characterization of Earth's features, but they also share a common limitation with other optical remote sensing technologies: the challenge of cloud formation in the atmosphere obstructing the satellites' capacity to monitor targets of interest. In this context, techniques such as semantic segmentation proves valuable in a broad range of space applications, e.g., from cloud recognition to wild-fire detection [11–18]. Segmentation can indeed serve as a cloud detection technique, categorizing image pixels as either cloudy or non-cloudy, essentially performing binary classification. As a mission example, after the launch in 2020 of the Phi-Sat-1 HS mission part of ESA's EOP initiative [1], a significant milestone was marked in 2021 when, for the first time, on-board AI

was introduced in a satellite for object detection, with the initial focus being the detection of clouds aboard the satellite. Phi-Sat-1 marked the first in-orbit inference with its convolutional CloudScout Deep Learning (DL) model for cloud detection [11, 14]. The mission’s imager, HyperScout-2, captures the Visible and Near-Infrared (VNIR) and Thermal Infrared (TIR) spectral ranges, and subsequently deploys data processing via AI models in its on-board configurable platform facilitating updates for its algorithms in flight [1, 12]. These in-orbit updates rely on an embedded configurable Commercial off-the-shelf (COTS) platform, which is based on a Vision Processing Unit (VPU) [12, 19]. Furthermore, beyond the Phi-Sat-1 mission, the literature [13] also extends cloud segmentation to image data of the missions Sentinel-2B (MSI) and FACSAT-1 (RGB) [20]. For instance, the state of the art [13] deploys a satellite data priority system to compute the cloud coverage level via DL-based segmentation on microcontrollers (MCUs), which determines the image downlink priority. Furthermore, the literature demonstrates that cloud detection can enhance data management aboard satellite platforms as presented next. On the one hand, selective HSI compression methods may be applied to cloud segments via CCSDS-123.0-B-2 to reduce their encoding rate [21, 22], while other methods like Compressed Sensing (CS) can also be employed to handle cloudy data, where CS proves particularly advantageous for satellites as it transfers computational complexity from orbit to mere ground-based reconstruction [23, 24]. Therefore, segmentation can lead to selective compression reducing the bit rate of data segregated as cloudy, or its absolute removal by data screening [12]. Consequently, this streamlines data postprocessing and enables the satellite to downlink, for instance, only valuable non-cloudy data, thus optimizing the usage of the often limited communication channel [13]. On the other hand, on-board cloud segmentation can additionally play a role in reducing decision-making latency, increasing satellite autonomy with more optimal on-board operations [12, 13, 15, 25–28]. Furthermore, from a broader perspective, the models first trained for cloud binary segmentation can be trained again to solve more complex problems instead, e.g., multi-class segmentation, where each image pixel is assigned to one of various categories. To further illustrate the importance of AI-powered cloud and multi-class segmentation for space applications, we next employ a particular small satellite mission as an example case. Namely, for Earth observation initiatives such as HYPSON-1 (HYPer-spectral small Satellite for Ocean observation) [5], the reduction in decision-making latency is especially im-

portant for time-sensitive remote sensing applications, such as early event warnings. HYPSON-1 focuses on timely detection of marine phenomena such as Harmful Algal Blooms (HABs), which can lead to significant mortality of farmed salmon. To this extent, in-orbit segmentation for adequate on-board data management can play a crucial role in achieving prompt management responses to mitigate adverse effects in such scenarios. In the context of multi-class segmentation, by segregating the data along various categories of interest, on-board AI can activate other subsequent agents in observational hierarchies monitoring the environment at multiple spatial, spectral and temporal scales with e.g. drones and marine vessels [5, 29, 30], where the HYPSON-1 satellite may serve as the space segment of an observational pyramid. However, handling increasingly advanced tasks on satellites, such as segmentation of growing complexity, is feasible only when the COTS components within the satellite’s payload are appropriately designed and optimized. Some COTS platforms provide benefits by accelerating, with high power efficiency, the repetitive operations commonly found in DL networks [1, 14, 19, 25]. Indeed, to enable AI applications in satellites, the literature explores various COTS hardware from the conventional MCUs [13] to the high-performance VPUs aboard Phi-Sat-1, Field-Programmable Gate Arrays (FPGAs) on board HYPSON-1, Tensor Processing Units (TPUs), Graphics Processing Units (GPUs), and other dedicated accelerators [1, 10, 11, 31–33].

To our knowledge, the existing literature in the field of cloud detection on board satellite platforms does not compare how different shallow and deep learning models, including distinctions like 1D vs. 2D-CNN-based models, influence the performance and complexity of cloud segmentation. Furthermore, the field also overlooks the effects of reducing the number of spectral channels, particularly in MSI/HSI data, on models for cloud segmentation. The existing literature lacks comparisons of key aspects, such as whether on-board AI for cloud detection, is better applied to raw data or L1b calibrated radiance data. It does not discuss how L1b calibration impacts segmentation results and does not provide justification for the optimal stage in the on-board data processing pipeline for image segmentation. Moreover, within the literature pertaining to cloud detection in HS satellite imagery, the primary emphasis naturally lies on binary segmentation, specifically distinguishing between the presence of clouds and non-cloudy data; in fact, as earlier mentioned, there are ranking systems that assess cloud levels based on the segmented outcomes. Nevertheless, none of the systems at the time of writ-

ing perform multi-class semantic segmentation for the simultaneous detection of clouds, sea, and land categories, which typically account for most of the variance in HS satellite imagery. The absence of sea-land-cloud segmentation systems impedes, as a result, the development of applications like priority ranking systems that can integrate the three categories into a unified ranker. In this work, we tackle the mentioned research gaps and utilize the HYPSON-1 mission as a case study, using its “Sea-Land-Cloud-Labeled Dataset” openly accessible in our prior article [34] (see data availability section at the end of this paper).

Following a methodology inspired by the data science CRISP-DM approach (CRoss Industry Standard Process for Data Mining) to ensure robust and reliable results, we train and compare 16 different Machine Learning (ML) and DL models. This extends the segmentation model baseline for HYPSON-1 first established in [34], and our research findings make contributions to the field as follows:

- We propose and fine-tune four new 1D-CNN and 2D-CNN models, with the aim of adapting them for on-board deployment on satellites. This optimization entails reducing the number of model parameters to achieve highly compact lightweight models while maintaining performance.
- For the case context of multi-class sea-land-cloud HS segmentation for the HYPSON-1 mission, we demonstrate that 1D-CNN models exhibit superior performance when compared to 2D-CNNs. Indeed, our optimized 1D-CNN lightweight models, 1D-Justo-LiuNet and 1D-Justo-HuNet, consistently outperform other state-of-the-art models.
- We substantiate that segmenting L1b radiance data, as opposed to using raw sensor data, enhances the segmentation of the top-performing models.
- We explore the impact of channel reduction on sea-land-cloud segmentation models.
- Finally, we propose a case example consisting of an image ranking system intended for downlink prioritization based on sea, land, and cloud coverage.

2. Methodological Background

2.1. Data Source: A Hyperspectral Labeled Dataset from HYPSON-1

We employ the “Sea-Land-Cloud-Labeled Dataset” from HYPSON-1 [34] (see data availability section). The

dataset consists of pixel-level labels for 25 million pixels across 38 scenes captured by HYPSON-1, where each HS image has spatial dimension of 956×684 pixels. Each pixel, contains a spectral signature of 120 channels covering the 400 to 800 nm range in the VNIR spectrum, with approximately 5 nm spectral resolution [5, 29]. The dataset consists of diverse scenes from various environments and provides raw data and L1b calibrated radiance for comparison with other HS missions. The dataset includes expert pixel-level annotations for three classes: “sea”, “land”, and “clouds”. The dataset exhibits a slight class imbalance with 37.01% pixels representing sea, 40.14% representing land, and 22.85% representing clouds/overexposed areas.

2.2. Channel Reduction Preprocessing

Following the common practice to inspect the data features prior to training ML and DL models, we next identify any unusual channel features that may require correction. In the sea-land-cloud dataset [34], we observe that the first four channels with wavelengths $\lambda=388, 391, 395, \text{ and } 399$ nm (visible blue spectrum) exhibit data samples equal to 0 for all the dataset HS images. We observe that this phenomenon occurs only to the L1b radiance, however, it is not present in the raw sensor data. This suggests that the occurrence of zero values in the first channels is a result of the radiometric calibration procedures applied by [34] following [35]. Furthermore, we observe that the dataset, near its wavelength $\lambda=760$ nm (oxygen A-band within the NIR spectrum), presents a sharp decline in light intensity which is attributed to the significant light absorption by the atmosphere’s oxygen at this wavelength [36, 37]. In summary, we exclude first wavelengths $\lambda=388, 391, 395, \text{ and } 399$ nm, and we also exclude the wavelengths in close proximity to $\lambda=760$ nm, namely, $\lambda=758, 761, 765, \text{ and } 768$ nm. As a result, the dataset’s original 120 channels are reduced to 112. The 112 channels, after undergoing min-max normalization, are the ones we employ for training the ML and DL models in the subsequent methodology. Since this work additionally studies the impact on the segmentation outcomes when significantly reducing the number of channels for the particular context of sea-land-cloud HSI segmentation, we use the 112-channel data to create a new dataset containing only 3 channels as detailed in [Appendix A](#).

2.3. Segmentation Modeling

2.3.1. Processing of 1D vs 3D Data

Our method involves training 16 distinct ML and DL models that are considered of interest for in-orbit deployment, with a particular emphasis on DL models,

as they are often better suited to capture more complex data relationships. To train the models, we maintain the same data split used in our prior article [34], allocating 30 HS images for training (79%), 3 images for validation (8%), and 5 images for testing (13%). Furthermore, we employ a deployment set of 30 additional HS images, also from the sea-land-cloud dataset, to test the best-performing model’s ability to generalize to further new unseen data. Additional details such as the specific image identifiers for the data split are provided in the supplementary material (see data availability section).

The ML and DL models presented in this work handle the data in either one-dimensional (1D) or three-dimensional (3D) formats. On the one hand, when we refer to 1D processing, it implies that the models make predictions solely based on spectral characteristics, disregarding any nearby spatial context. Examples of such models include 1D-CNNs based on 1D convolutions, where the input consists of a spectral signature with no spatial context. Henceforth, we refer to these types of models as 1D models. However, when we refer to 3D processing, it signifies that the models concurrently analyze multiple adjacent spatial pixels, incorporating the hyperspectral datacube with both spectral (1D) and spatial (2D) information to predict the class for each pixel. Models like 2D-CNNs, that we refer henceforth as 2D models serve as examples, where the input is a 3D image containing both spatial and spectral data. Convolutional layers in 2D-CNN models operate by first applying 2D convolutions individually between each spectral channel and its respective neural kernel component. Subsequently, they aggregate the 2D convolutional results stacked in the spectral dimension to produce a final 2D feature map. Finally, we describe in [Appendix B](#) the arrangement of the data dimensions required for training and inference. In the appendix, we offer e.g. information about how the images are divided into 3D patches for 2D-CNNs and the size of the patches used.

2.3.2. Baseline Segmentation Models

As a starting point, we begin using simple baseline models consisting of traditional ML algorithms as they are often more interpretable than deep neural networks. For convenience, during this initial phase, the models process 1D data (spectral signatures), which is a simpler processing strategy compared to handling 3D image patches. The initial ML baseline consists of Stochastic Gradient Descent (referred henceforth as 1D-ML/SGD), Gaussian Naïve Bayes (1D-ML/NB), Linear Discriminant Analysis (1D-ML/LDA), and Quadratic Discriminant Analysis (1D-ML/QDA). Next, we incorporate multiple state-of-the-art DL models for 3D patch pro-

cessing, such as NU-Net [38] and NU-Net-mod [13], previously employed in satellite imagery for cloud detection in RGB (FACSAT-1) and MSI (Sentinel-2B). Furthermore, we incorporate additional DL models, namely C-UNet and C-UNet++, distinguished by the authors [39] as *lightweight* for their minimal parameter count and low computational requirements, making them well-suited for deployment on satellites. C-UNet and C-UNet++ are compact versions of the standard encoder-decoder U-Net architecture [40]. The subsequent literature [41] building upon [39], explores C-UNet and C-UNet++ models suggesting their possible use for segmentation in HS missions such as HYPSON-1. However, the method in [41] involves training on only two limited HS images, the conventional Pavia Centre and AeroRIT scene, which use sensors different from HYPSON-1 and do not include any cloud or oceanic data, which is of particular interest for ocean observation in HYPSON-1. In our work, we refer to the compact models in [41] as 2D-CUNet and 2D-CUNet++, and to their further reduced versions in [41] as 2D-CUNet Reduced and 2D-CUNet++ Reduced. Moreover, we add models from [42], which [42] refers to as the FAUBAI model with reference to the FAUBAI project that focuses on segmentation for HS imagery for its possible future use in satellites. We refer to the networks in [42] as 2D-UNet FAUBAI and to its reduced version as 2D-UNet FAUBAI Reduced. Although Netteland [42] recommends any of these two networks for tasks such as cloud segmentation in HS satellite imagery, we note that similarly to [41], Netteland [42] conducted model testing only on a restricted set of four conventional HS images, namely, Pavia Centre, Pavia University, Salinas, and Indian Pines, which do not contain cloud or oceanic data.

2.3.3. Customised Segmentation Models

2.3.3.1 Review of 1D-CNNs: *Liuetal*, *Huetal*, and *LucasCNN*

The *Liuetal* [43], *Huetal* [44] and *LucasCNN* [45] 1D-CNN models have been used before for data analysis in soil spectroscopy to segment various soil texture classes in HS data. Additionally, in our previous article [34], we verified that a modified version of *Liuetal* achieved high performance in satellite HS imagery, surpassing the state-of-the-art in soil spectroscopy [45]. In this work, we find *Liuetal*, *Huetal*, and *LucasCNN* of interest also for in-orbit inference due to their simple 1D processing approach. Therefore, assuming 112 spectral channels and 3 classes to segment, in [Table I](#) we show the parameter counts for the three models. The parameter counts are in the order of tens of thousands with the

Liuetal having the lowest number of parameters among the three. Following our pursuit of further reducing the parameter count to merely a few thousands, more convenient for inference aboard satellites, in the next sections we accordingly modify the soil models in [45], while aiming to preserve their performance.

2.3.3.2 Ablation Study

To adapt the soil models for deployment in space by reducing their trainable parameters while not degrading the models’ performance, we initially investigate the relevance of each neural layer and subsequently conduct hyperparameter fine-tuning. In the first column of Table I, we list the state-of-the-art soil models in italic font, while our customized models are listed in bold. We also differentiate our models by the addition of the term “Justo” to their names. In the subsequent columns of the table, for our models, we utilize bold font to highlight the hyperparameters that we modify compared to the soil models.

Taking into account the promising nature of 1D-CNNs as lightweight models for on-board deployment, we focus the hyperparameter optimization exclusively on them, and we omit the optimization for 2D-CNN models. The modifications to the hyperparameters in Table I further discussed in the following section, are a direct outcome of the hyperparameter fine-tuning process next. Namely, we begin by assigning them first intuitive values that can yield acceptable performance. Then, we conduct a search using a hyperparameter grid, based on the initial values, to identify the optimal combination of hyperparameters. To accommodate the high dimensionality of HSI data, we randomly choose only 2 million spectral signatures (approximately 10% of the training set) to reduce the time needed for the grid search. Additionally, while evaluating the grid models through cross-validation, we restrict the evaluation to only two fold permutations to decrease computation time further.

2.3.3.3 Introducing New Lightweighth 1D-CNNs: *1D-Justo-LiuNet*, *1D-Justo-HuNet* and *1D-Justo-LucasCNN*

The hyperparameter optimization process in previous section aims to achieve optimal accuracy, but we emphasize that the minimization of parameter counts for optimal in-orbit deployment is still the primary focus of our method. In this context, in our prior article [34], we presented a modified version of the *Liuetal* network resulting in 124,163 parameters, which might be con-

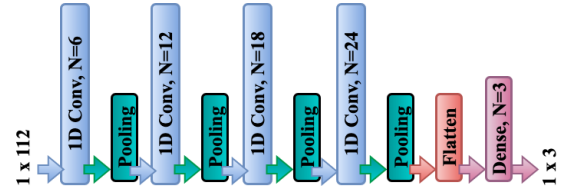


Figure 1: Lightweight 1D-Justo-LiuNet architecture for on-board segmentation. As an illustration, the block diagram employs 112 input channels for a single pixel. The network generates three detection probabilities, corresponding to sea, land, and clouds, respectively.

sidered large for in-flight deployment. However, our results demonstrated superior performance when contrasted with the *Liuetal* model [45]. We consider that the large parameter count in [34], which did not result in model overfitting, likely contributed to the significant performance improvement over the state-of-the-art. Nevertheless, in this article, our goal is to once again outperform the state-of-the-art, while also reducing the parameter count, in contrast to our previous work [34]. Indeed, we aim to achieve a parameter count even lower than the count of the *Liuetal* model in Table I. Therefore, we next present the 1D-Justo-LiuNet in Fig. 1, which achieves 80% reduction in parameters compared to *Liuetal* (22,755) [45]. 1D-Justo-LiuNet is adapted to only 4,563 parameters, as shown in Table I. This reduction is accomplished by first following the approach in our prior article [34], suggesting to start with a base seed of convolutional kernels and progressively increase the kernel counts (denoted as N in Table I) based on the seed multiplied by factors of 2, 3, and 4 as the network deepens. In this work, we however start with a small seed of 6 kernels, instead of 32 as in [34], to achieve the substantial 80% reduction in the model’s parameter count. Moreover, as we did in our previous publication, we double the kernel size (denoted as K in Table I) compared to [45] in order to compensate for the reduction in the kernel counts, thereby ensuring that performance is not adversely affected.

For the *Huetal* model also in [45], the high parameter count in Table I is mainly a result of a fully connected layer with numerous neurons preceding the output classification layer. We refine the model, naming it 1D-Justo-HuNet, by reducing 70% the neural units in the fully connected layer. By implementing additional modifications such as reducing the number of convolutional kernels and adjusting their kernel size, we attain a significant 90.50% reduction in parameter count (9,543). As for *LucasCNN* [45], our model, 1D-Justo-LucasCNN, follows the same approach applied to *Huetal* to reduce the parameter count, i.e., we significantly

Table I: Overview of hyperparameters and parameter count for 1D-CNN segmentation models.

Model	Parameter Count	Layers	Parameters
<i>Liuetal</i>	22,755	Hidden: 4 1D Convolutions & 4 Max Poolings Output: Flatten & 1 Dense	Hidden/Convolutions: $N=32,32,64,64$; $K=3$; $Act.=ReLU$ Hidden/Poolings: $\div 2$ Output/Dense: $N=3$; $Act.=Softmax$
1D-Justo-LiuNet	4,563	Hidden: 4 1D Convolutions & 4 Max Poolings Output: Flatten & 1 Dense	Hidden/Convolutions: $N=6,12,18,24$; $K=6$; $Act.=ReLU$ Hidden/Poolings: $\div 2$ Output/Dense: $N=3$; $Act.=Softmax$
<i>Huetal</i>	100,663	Hidden: 1 1D Convolution & 1 Max Pooling Output: Flatten & 2 Dense	Hidden/Convolution: $N=20$; $K=12$; $Act.=Tanh$ Hidden/Pooling: $\div 2$ Output/Dense 1: $N=100$; $Act.=Tanh$ Output/Dense 2: $N=3$; $Act.=Softmax$
1D-Justo-HuNet	9,543	Hidden: 1 1D Convolution & 1 Max Pooling Output: Flatten & 2 Dense	Hidden/Convolution: $N=6$; $K=9$; $Act.=Tanh$ Hidden/Pooling: $\div 2$ Output/Dense 1: $N=30$; $Act.=ReLU$ Output/Dense 2: $N=3$; $Act.=Softmax$
<i>LucasCNN</i>	80,155	Hidden: 4 1D Convolutions & 4 Max Poolings Output: Flatten & 3 Dense	Hidden/Convolutions: $N=32,32,64,64$; $K=3$; $Act.=ReLU$ Hidden/Poolings: $\div 2$ Output/Dense 1: $N=120$; $Act.=ReLU$ Output/Dense 2: $N=160$; $Act.=ReLU$ Output/Dense 3: $N=3$; $Act.=Softmax$
1D-Justo-LucasCNN	25,323	Hidden: 1 1D Convolution & 1 Max Pooling Output: Flatten & 3 Dense	Hidden/Convolution: $N=16$; $K=9$; $Act.=Tanh$ Hidden/Pooling: $\div 2$ Output/Dense 1: $N=30$; $Act.=Tanh$ Output/Dense 2: $N=5$; $Act.=Tanh$ Output/Dense 3: $N=3$; $Act.=Softmax$
2D-Justo-UNet-Simple	7,641	Hidden: 3 2D Convolutions & 2 Max Poolings & 2 Upsamplings Output: 1 2D Convolution * Batch normalization after all 2D Convolutions	Hidden/Convolutions: $N=6,12,6$; $K=3 \times 3$; $Act.=ReLU$ Hidden/Poolings: $\div 2$ Hidden/Upsamplings: $\times 2$ Output/Convolution: $N=3$; $K=3 \times 3$; $Act.=Softmax$

reduce the neural units in the two dense layers before the classification layer. Specifically, *LucasCNN* has 280 neural dense units, while 1D-Justo-LucasCNN reduces the units by 87% to just 35 neurons. Furthermore, 1D-Justo-LucasCNN includes other adjustments, such as transforming the 4-scale *LucasCNN* into a single-scale network, significantly reducing the number of convolutional kernels while tripling the kernel size, and employing a hyperbolic neural activation instead of a linear function result of the hyperparameter optimization process. Table I illustrates a 68.41% reduction in parameter count (25,323) achieved by 1D-Justo-LucasCNN. The architectural details (as in Fig. 1) of the 1D-Justo-HuNet and 1D-Justo-LucasCNN are available in the supplementary materials, which also include the software codes to reproduce the models.

2.3.3.4 Introducing a New Lightweight 2D-CNN: 2D-Justo-UNet-Simple

Finally, to achieve lightweight models with reduced parameters, not only for 1D-CNN models as in previous section, but also for 2D-CNN architectures, we introduce: 2D-Justo-UNet-Simple with 7,641 parameters, as shown in Table I. The 2D-Justo-UNet-Simple consists of a compressed version of the encoder-decoder U-Net architecture with only 2 scales (as opposed to the typical 4 scales in U-Nets [40]), with a bottleneck level consisting of only 12 convolutional kernels. Additionally, following each 2D convolution operation and before pooling or upsampling, we insert batch normalization before the rectified linear activation to enhance model generalization and mitigate potential gradient vanishing or exploding effects during training. We note that in the decoder's expanding path, we employ upsampling layers as an alternative to utilizing operations like transposed

convolutions. While transposed convolutions may enhance performance, they also lead, however, to an increase in the number of trainable parameters. The software code and architectural details (as in Fig. 1) of the 2D-Justo-UNet-Simple are provided in the supplementary materials of this article.

2.3.4. Training Procedure

The DL models (implemented with Keras) are trained on an NVIDIA RTX A4000 GPU to increase the training speed, while the ML models (implemented with scikit-learn) are trained on a 13th Gen Intel(R) Core (TM) i9-13900K CPU, which results in a slower training process relying on CPU computation. We employ supervised learning to train the ML and DL models, with a special focus on the training process of DL models. This is crucial because, due to their larger number of parameters, DL models are more susceptible to overfitting than ML models.

We start by using the 112-channel dataset (from Section 2.2) to train the 1D and 2D models. However, when working with the 3-channel dataset (from Section 2.2 and Appendix A), we exclusively focus on training 2D models instead of 1D models. This decision is primarily based on the fact that 1D models do not take spatial information into account and rely solely on the spectral features, which, in this case, comprise only 3 channels. Furthermore, 1D-CNN models can face challenges related to the diminishing channel features as the network depth increases. Namely, when working with only three channels, the reduction in features is so pronounced that, in the first layers of the network, the processed features already diminish to zero, rendering prediction for three channels unfeasible.

In our training procedure, we initially select high-level parameters like the number of epochs and the batch size, followed by the choice of the lower-level hyperparameters previously discussed. In terms of high-level parameters, for both 1D-CNN and 2D-CNN models, we find that our dataset benefits from small batch sizes, increasing the frequency of updates in trainable parameters, but also extending the training time. As regards to batch size during inference, Keras dynamically selects the batch size for optimal memory efficiency. In addition, we find that it is advisable to utilize a small number of training epochs to prevent overfitting. Specifically, for 1D-CNNs, we use 2 epochs and a batch size of 32 pixels, while for 2D-CNNs, we opt for 3 epochs and a batch size of 4 patches. Furthermore, we employ the Adam optimizer with its default parameters to minimize the categorical cross-entropy loss, while us-

ing accuracy as evaluation metric in the training and validation sets.

To evaluate the model’s performance at the end of each training epoch, we focus on the overall validation accuracy (validation set imbalance: 51.25%, 28.13%, and 20.62% for sea, land, and clouds, respectively), and we aim to achieve an empirical validation accuracy of around 0.90 during training. After completing the last training epoch, we evaluate false positives and false negatives (inversely proportional) by treating the segmentation of each class as a binary classification problem. In this context, we note that the significance of the false positives and false negatives varies per class, as elaborated further in the upcoming section. However, we note in advance that we aim for a reasonably balanced trade-off between false positives and false negatives across sea, land, and cloud classes before selecting the final trained model. Therefore, we consider false positives and false negatives intuitively during our training procedure, but we acknowledge more rigorous methods that focus on minimizing either false positives or false negatives by adjusting decision thresholds. The adjustments can involve, for instance, altering the decision boundary during the categorical class assignment based on different probability thresholds, consequently impacting the false positives and false negatives for each class. Additionally, applying penalties within the loss function to address specific class misclassifications can also affect false positives and false negatives. However, in our work, we consider sufficient to predict the categorical classes during inference by simply selecting the class with the highest probability, while equally penalizing all classes during training as the dataset imbalance is moderate. Finally, while quantization of trainable parameters certainly contributes to further compacting lightweight models [12], we emphasize that we do not perform parameter quantization in this article. The literature [15] demonstrates that in certain cases, where highly compressed light models are utilized (as in this work), quantization is unnecessary since the reduction in parameter count alone may be sufficient for in-orbit deployment. Furthermore, the effects of quantization can be highly dependent on the processing architecture.

In the supplementary material of this article, we provide the trained model files with the learned parameters (46 distinct files). Additionally, we include a user-friendly software program we develop, offering an intuitive graphical user interface for conducting oceanic-terrestrial-cloud segmentation on HYPSON-1 imagery.

2.4. Segmentation Performance Metrics and Proposed Example Application

2.4.1. Proposed On-Board Sea-Land-Cloud Ranking System

Before introducing the metrics to evaluate the segmentation outcomes, we next introduce example applications to study the utility of the sea, land, and cloud segments in increasing the satellite’s autonomy, while reducing data postprocessing and decision-making latency. Several performance metrics discussed in the following section are indeed based on the proposed example applications. Namely, in Fig. 2 we suggest a novel sea-land-cloud ranking system intended for in-orbit deployment. The system prioritizes HS images for downlink based on sea, land, and cloud coverage levels, ensuring high-priority transmission. The images are arranged in ascending order of cloud coverage levels, descending order of sea coverage levels, and also decreasing order of land coverage levels, with the first positions reserved for images of higher downlink priority. Unlike existing ranking systems that target only clouds [13], our proposed approach is the first of its kind for HSI-equipped satellites, simultaneously locating and ranking sea, land, and clouds within priority queues. In Fig. 2, we also suggest other on-board use cases that further highlight the usefulness of the sea-land-cloud segments. The use cases include alternatives such as discarding or applying selective lossy compression to non-essential pixels to optimize the utilization of the Shannon channel capacity, particularly vital for satellites like HYPSON-1 that may be operating with limited line-of-sight (LOS) towards ground stations [29].

2.4.2. Performance Metrics

Regarding performance metrics, we utilize a range of metrics to assess the quality of the segmented images on the test set (prior to generalization tests in the deployment set) in order to evaluate the models’ performance after training. First, our primary focus is on average accuracy, a widely used metric for evaluating segmentation models. Unlike overall accuracy, this average metric is particularly convenient for imbalanced test sets, providing a more realistic assessment. Furthermore, adhering to the literature of cloud detection in satellite imagery [12, 14], we also calculate the false and true alarm ratios, for each class in this work. Finally, in our supplementary material supporting further the conclusions of our work, we present additional state-of-the-art metrics that we consider secondary in importance for our purpose compared to the previous metrics. Namely, the F-1 score in addition to the overall accuracy.

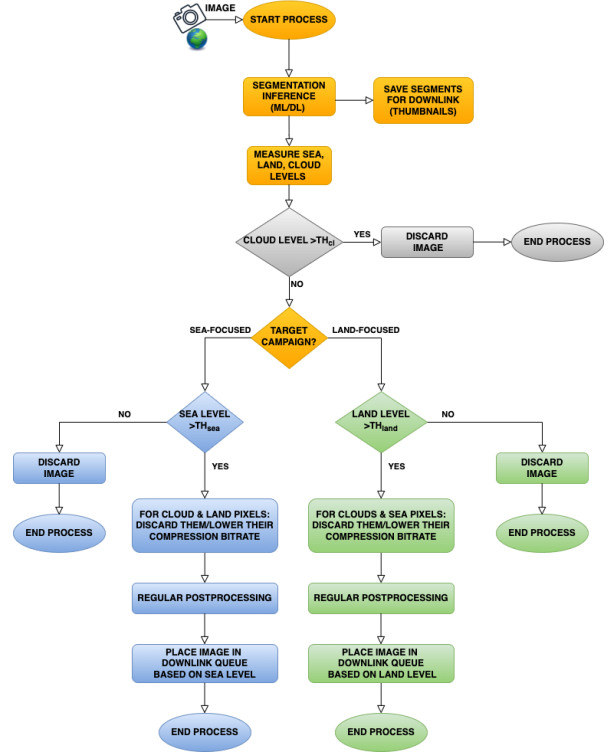


Figure 2: An intelligent on-board processing pipeline integrating a ranking system based on sea-land-cloud segmentation. TH_{cl} , TH_{sea} , and TH_{land} represent thresholds configured at the ground center to regulate data management during in-flight operations.

Furthermore, we introduce additional performance metrics for the ranking system to assist the evaluation of the ML and DL models. To assess the predicted rankings for each coverage level, we use the Spearman’s rank correlation coefficient to measure the relationship between the predicted and ground-truth rankings, with values ranging from -1 to 1 , representing a perfect match at the upper end. Moreover, we compute the Mean Absolute Error (MAE) for each coverage level, treating each level similar to a separate regression task. To maintain simplicity, we include the details about MAE in our supplementary materials.

In the context of on-board data management proposed in Fig. 2, the false alarm ratios due to misclassifications indicate either the potential loss of data or the transmission of irrelevant data during downlink, as explained next. In cloud segmentation, the True Positive Ratio (TPR) involves correctly detecting cloudy pixels, while the True Negative Ratio (TNR) relates to recognizing non-cloudy data with potential value. The False Positive Ratio (FPR) is crucial because it indicates misclassified pixels, wrongly identified as clouds but that ac-

tually correspond to sea or land data. Following Fig. 2, these misclassifications can result in the discard or selective lossy compression with lower bitrate of valuable data. On the other hand, the False Negative Ratio (FNR) is less critical than FPR, as it does not involve data loss or data degradation, but only a less efficient usage of the downlink channel transmitting undetected pixels actually corresponding to clouds. In the context of sea segmentation, true positives signify correct identification of valuable sea data, while true negatives correctly recognize non-relevant data for potential deletion or compression. In sea-focused campaigns, FNR is critical, as it deals with misclassified sea-related pixels, potentially leading to loss of valuable data or degradation. In contrast, FPR is of less significance since its impact lies merely in downlink efficiency with the transmission of irrelevant pixels (clouds or land), rather than causing any actual data loss. The same analysis and conclusion apply when examining the context of land segmentation. In short, without taking into account the earlier suggested reasonable compromise between false positives and false negatives, for both sea and land categories, FNR has priority over FPR due to valuable data loss or degradation in the case of high FNR. However, for cloud data, FPR is critical as it leads to irreversible data loss or lossy compression, with FNR affecting merely downlink efficiency.

3. Results

We conduct model training using 112 channels of both raw sensor data and L1b calibrated radiance, and we discuss the segmentation of raw and L1b radiance in Section 4. For L1b radiance, we present the outcomes of the segmentation models in Table II, where we utilize bold font to accentuate our models. The table displays the models' performance for segmentation, with the primary metric being the average accuracy across the sea, land, and cloud classes. Additionally, to assess the sea-land-cloud segmentation performance for the context of the proposed on-board ranking system, we also include the average Spearman's rank coefficient. In particular, the average Spearman's coefficient across the respective rankings based on sea, land, and cloud coverage levels is presented in Table II. Moreover, we also include information about the network's parameter count to offer insights of the potential memory demands for in-orbit deployment. In addition, we provide the average inference time per HS image measured in our testing setup on ground, on the NVIDIA RTX A4000 GPU (for DL), and on the 13th Gen Intel(R) Core (TM) i9-13900K CPU (for ML). From the numbers presented in

Table II, we sort the models in Table III based on their respective metrics. In Table III, we first sort the models solely based on their average accuracy, from highest to lowest, and subsequently, we sort them in the following columns, first by the Spearman's coefficient (highest to lowest), then by the number of parameters (lowest to highest), and finally by inference time (shorter to longer). Therefore, the first rows in the table represent the top models in the test set for each respective metric. However, while average accuracy offers a general overview on segmentation performance across the sea, land, and cloud classes, it may obscure poor model performance in specific classes. To address this, we offer additional insights into individual class performance by presenting their respective binary false detection ratios. Namely, in Figs. 3, 4, and 5, we provide a comparative visual representation of false alarm ratios for the binary segmentation of each distinct class. We note that the top-performing models get positioned in the lower-left corners, indicating the optimal trade-off balance between low false positives and low false negatives. Within the context of the example case presented in Fig. 2, the graphs illustrate the false alarm ratio on the Y-axis corresponding to the loss (or degradation) of valuable data, while the X-axis pertains to a false detection ratio that reflects the *inefficient* utilization of the downlink channel. In relation to this trade-off, we stress that while minimizing the loss of valuable data remains crucial, we also highlight the importance of maintaining an acceptable downlink efficiency.

Finally, our experiments conclude by training again the models using the 3-channel dataset instead. We employ the dataset to assess the impact of channel reduction on the segmentation models' performance, parameter count, and inference times, as shown in Table IV. We note that the table omits the 1D models due to the 3-channel dataset's restricted spectral information, as mentioned earlier in Section 2.3.4. Moreover, the empirical results are further confirmed by training once again the models with a set of three channels different from the ones in Section 2.2/Appendix A. The new results align with the previous findings and for simplicity, we include the new figures in the supplementary material.

Finally, as previously noted, the dataset predominantly contains instances of sea and land, with clouds representing the minority class. Consequently, the test set also exhibits a lower proportion of cloud data (14.13%), in contrast to sea (39.01%) and land (46.85%). We recognize this as a limitation that demands future refinement. Therefore, to mitigate the impact of the class imbalance during the testing phase,

Table II: Metrics for segmentation models trained using 112 spectral channels.

Model	Accuracy	Spearman's Coefficient	Parameter Count	Inference Time [ms]
1D-ML/SGD	0.91	0.90	-	72
1D-ML/NB	0.71	0.27	-	1,234
1D-ML/LDA	0.89	0.93	-	190
1D-ML/QDA	0.89	0.63	-	2,024
1D-Justo-LiuNet	0.93	1.00	4,563	15,136
1D-Justo-HuNet	0.91	1.00	9,543	10,966
1D-Justo-LucasCNN	0.91	0.90	25,323	11,554
2D-NU-Net-mod	0.8	0.83	32,340	364
2D-NU-Net	0.81	0.77	40,332	374
2D-CUNet	0.72	0.83	67,299	272
2D-CUNet++	0.83	0.77	24,619	294
2D-CUNet Reduced	0.76	0.90	22,019	270
2D-CUNet ++ Reduced	0.90	0.83	12,379	294
2D-UNet FAUBAI	0.88	0.90	26,534,211	462
2D-UNet FAUBAI Reduced	0.85	0.83	1,956,835	388
2D-Justo-UNet-Simple	0.92	0.93	7,641	318

Table III: Ranking of models' metrics from best to worst for segmentation models trained over 112 channels.

Ranking	Accuracy	Spearman's Coeff.	Parameter Count	Inference Time
1	1D-Justo-LiuNet	1D-Justo-LiuNet	1D-Justo-LiuNet	1D-ML/SGD
2	2D-Justo-UNet-Simple	1D-Justo-HuNet	2D-Justo-UNet-Simple	1D-ML/LDA
3	1D-ML/SGD	2D-Justo-UNet-Simple	1D-Justo-HuNet	2D-CUNet Reduced
4	1D-Justo-HuNet	1D-ML/LDA	2D-CUNet++ Reduced	2D-CUNet
5	1D-Justo-LucasCNN	1D-Justo-LucasCNN	2D-CUNet Reduced	2D-CUNet++
6	2D-CUNet++ Reduced	1D-ML/SGD	2D-CUNet++	2D-CUNet++ Reduced
7	1D-ML/LDA	2D-CUNet Reduced	1D-Justo-LucasCNN	2D-Justo-UNet-Simple
8	1D-ML/QDA	2D-UNet FAUBAI	2D-NU-Net-mod	2D-NU-Net-mod
9	2D-UNet FAUBAI	2D-CUNet	2D-NU-Net	2D-NU-Net
10	2D-UNet FAUBAI Reduced	2D-NU-Net-mod	2D-CUNet	2D-UNet FAUBAI Reduced
11	2D-CUNet++	2D-CUNet++ Reduced	2D-UNet FAUBAI Reduced	2D-UNet FAUBAI
12	2D-NU-Net	2D-UNet FAUBAI Reduced	2D-UNet FAUBAI	1D-ML/NB
13	2D-NU-Net-mod	2D-CUNet++	-	1D-ML/QDA
14	2D-CUNet Reduced	2D-NU-Net	-	1D-Justo-HuNet
15	2D-CUNet	1D-ML/QDA	-	1D-Justo-LucasCNN
16	1D-ML/NB	1D-ML/NB	-	1D-Justo-LiuNet

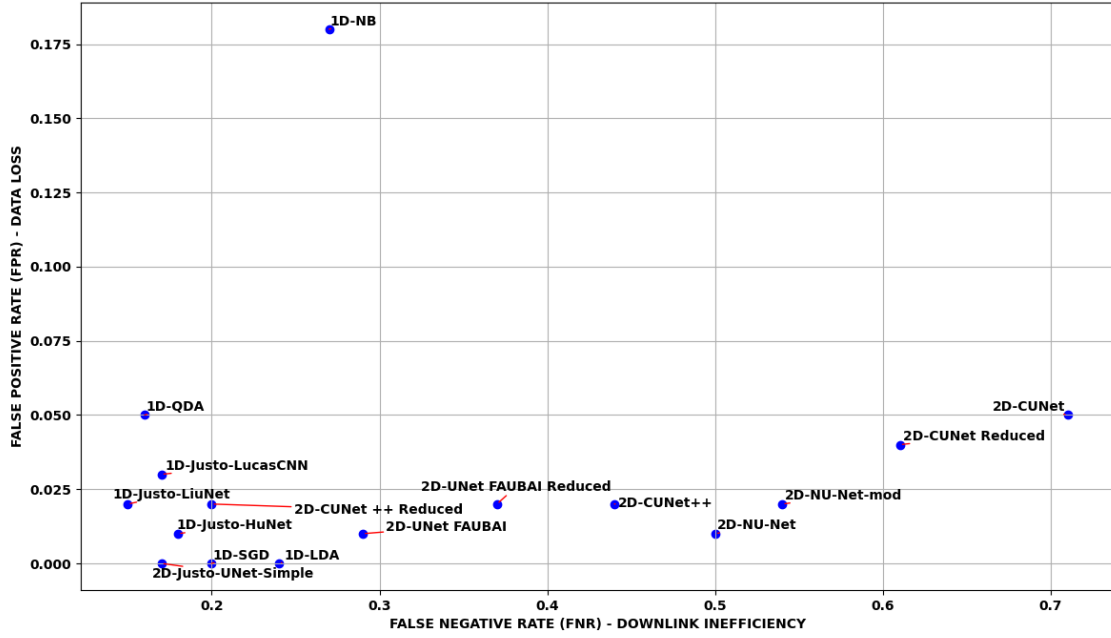


Figure 3: Comparison of false cloud detection ratios for segmentation models trained over 112 channels.

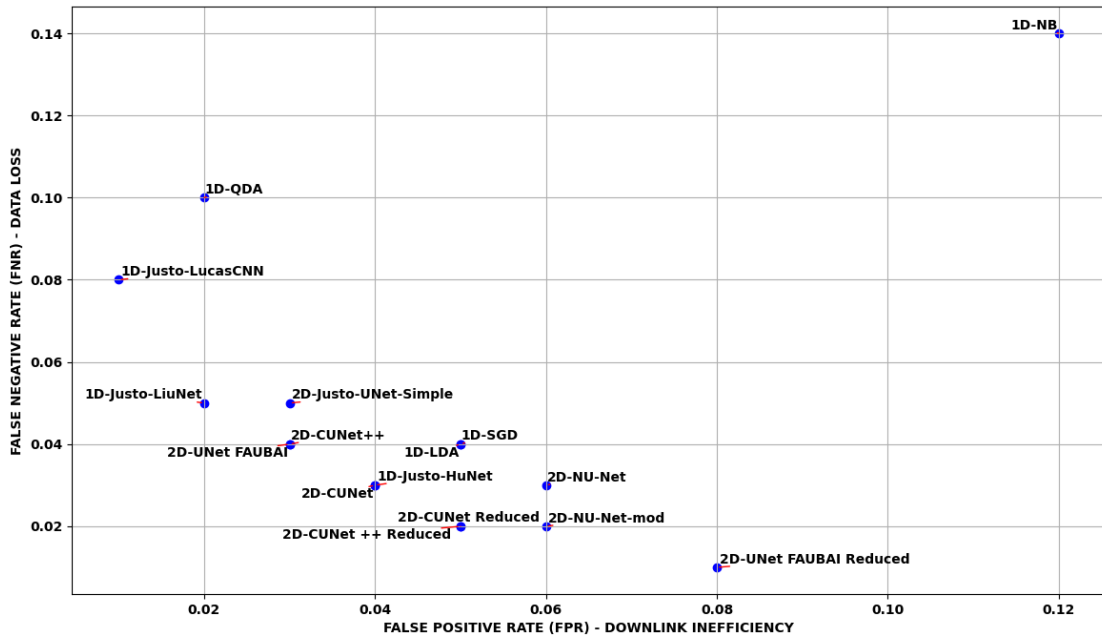


Figure 4: Comparison of false sea detection ratios for segmentation models trained over 112 channels.

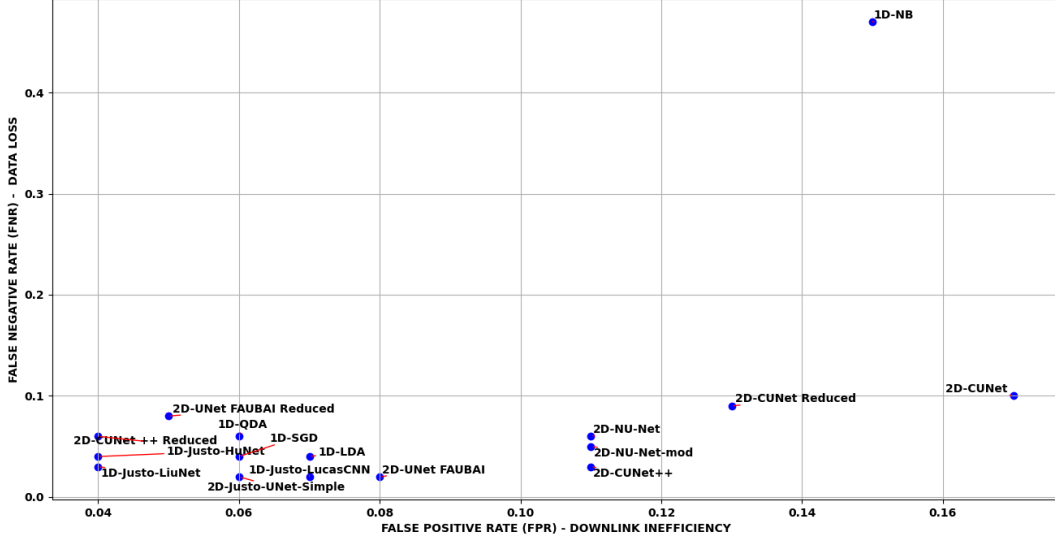


Figure 5: Comparison of false land detection ratios for segmentation models trained over 112 channels.

Table IV: Metrics for segmentation models trained using only 3 spectral channels.

Model	Accuracy	Spearman's Coefficient	Parameter Count	Inference Time [ms]
2D-NU-Net-mod	0.66	0.37	32,231	224
2D-NU-Net	0.80	0.53	32,375	192
2D-CUNet	0.86	0.83	59,451	162
2D-CUNet++	0.84	0.6	16,771	100
2D-CUNet Reduced	0.87	0.73	14,171	156
2D-CUNet ++ Reduced	0.84	0.83	4,531	122
2D-UNet FAUBAI	0.87	0.77	26,471,427	346
2D-UNet FAUBAI Reduced	0.85	0.57	1,941,139	230
2D-Justo-UNet-Simple	0.85	0.83	1,755	112

we conduct additional experiments. Namely, we perform inference on an additional on-ground deployment set, with 30 HS images, specifically designed to test the model's generalization on e.g. cloudy and overexposed images to further support the findings of our work, and we provide the complete results in the supplementary material. As an example, Fig. 6 provides a comparison of the segmentation outcomes of the 1D-Justo-LiuNet and the 2D-CUNet++ Reduced for a sample image from the deployment set.

4. Discussion

4.1. Results Analysis for Models Trained on 112 Channels

We first analyze the results for the models trained on 112 channels (Tables II and III). Our objective is to investigate how the utilization of the imaging spatial context by 2D models affects the sea-land-cloud segmentation across the test images. We assess the models' strengths and limitations in terms of performance, spanning from the average accuracy and the binary false alarm ratios to the Spearman's correlation coefficient for the ranking system. We finalise the analysis by discussing the model's parameter count and inference time, which are relevant metrics for on-board deployment.

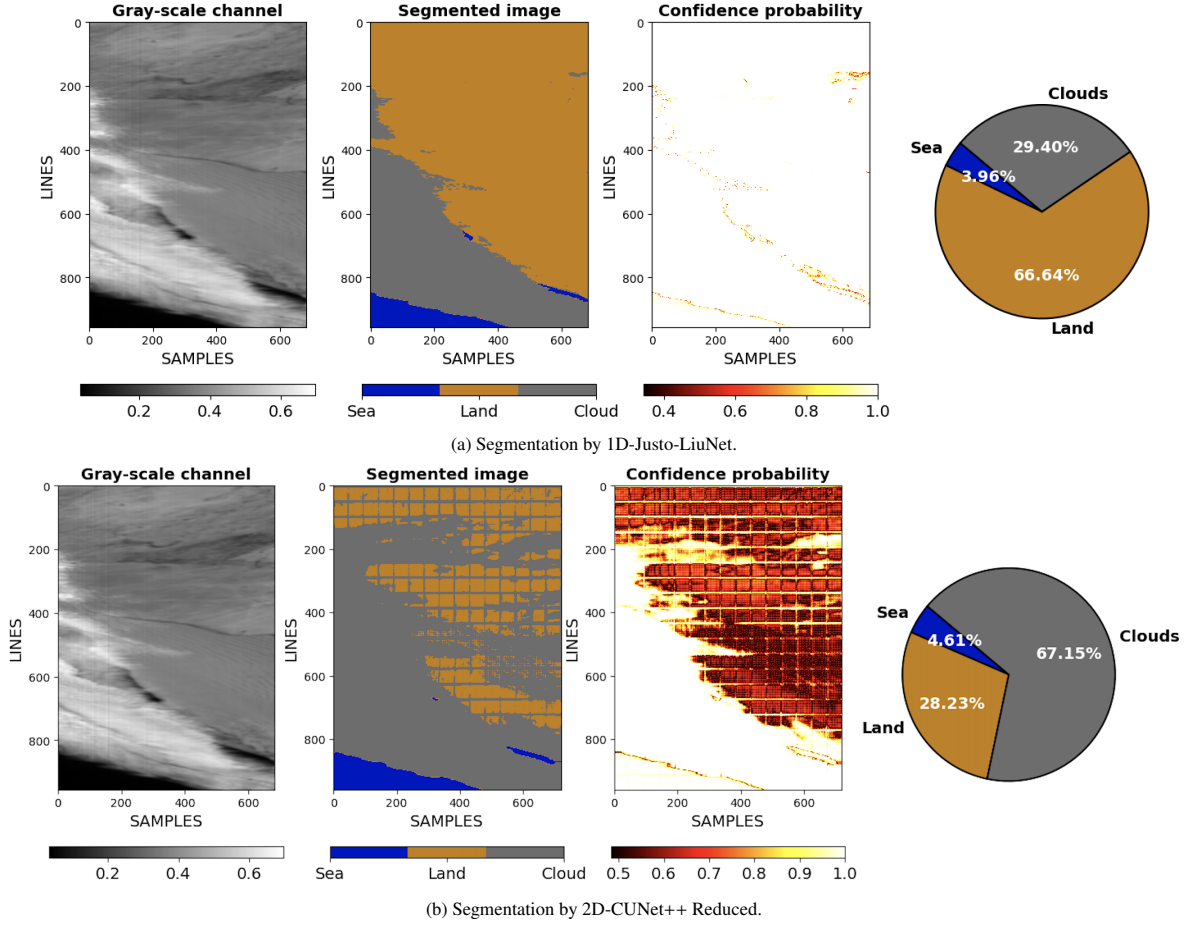


Figure 6: Segmentation results for a HYPSON-1 capture over the Namib desert in Namibia, Africa, close to the Gobabeb Namib Research Institute for dry land research. The approximate coordinates for this location are $23^{\circ}19'06.0''\text{S}$ latitude and $14^{\circ}44'21.8''\text{E}$ longitude. The grayscale image in (a) and (b) corresponds to the same L1b channel with a wavelength λ of 699.61 nm, close to NIR spectrum. The term SAMPLES denotes the swath width captured across the direction of satellite travel, while LINES indicates the number of scan frames collected along the satellite’s path. As stated in [5, 29], HYPSON-1’s spatial resolution in the across- and along-track directions is approximately 100 m x 600 m.

Prior to the analysis of the results, we intuitively formulate a hypothesis next, independent of the empirical findings. The hypothesis asserts that it is reasonable to anticipate better performance for 2D models compared to 1D models. This expectation arises because 2D models, unlike 1D models relying solely on spectral context, analyse a richer context comprising both spectral and spatial information. We next proceed to elaborate whether the empirical results substantiate such hypothesis.

4.1.1. Segmentation Performance (I): Average Accuracy

When examining the segmentation performance solely based on the average accuracy across sea, land, and cloud classes, we observe that our proposed model,

1D-Justo-LiuNet, achieves the highest accuracy of 0.93 in Table II. The result of a 1D model outperforming 2D models is not an exception, as four out of five models ranking among the top performers in accuracy in Table III are consistently 1D models. The only exception in this top five ranking is our 2D model, 2D-Justo-UNet-Simple, which achieves an accuracy of 0.92, closely approaching the performance of the 1D-Justo-LiuNet. Therefore, the findings lead to the conclusion that the initially expected hypothesis suggesting that 2D models would outperform 1D models does not hold valid in our experiments, as the 2D models exhibit worse performance. This phenomenon can be attributed to the fact that 1D models, unlike 2D using the spatial context, are not affected by the modest spatial resolution of HYPSON-1’s images while not suffer-

ing from the spatial variations that may be practically irrelevant and misleading for pixel-level segmentation. Instead, 1D models dedicate their efforts to analyzing exclusively the spectral context, which is, certainly, a powerful domain in HS imagery. Additionally, Table III demonstrates that our proposed models (1D-Justo-LiuNet, 2D-Justo-UNet-Simple, 1D-Justo-HuNet, and 1D-Justo-LucasCNN) outperform, in average accuracy, the state-of-the-art models under analysis, when trained on the HYPISO-1 dataset for sea-land-cloud segmentation. Indeed, we surpass models such as the 2D-NU-Net-mod, 2D-NU-Net, 2D-UNet FAUBAI, and 2D-UNet FAUBAI Reduced previously employed in the field of cloud segmentation for satellite remote sensing imagery. Finally, we highlight that the average accuracy of 1D-Justo-LiuNet (0.93), 1D-Justo-HuNet (0.91), and 1D-Justo-LucasCNN (0.91) also surpass the literature’s average accuracy for soil texture [45]. As a matter of fact, the state of the art achieves significantly lower average accuracy of 0.59, 0.61, and 0.56 for *Liuetal*, *Huetal*, and *LucasCNN*, respectively.

4.1.2. Segmentation Performance (II): The Effect of L1b Radiance Calibration

The models in Table II are trained on L1b calibrated radiance data. L1b radiance is one of the standard data formats in HS imagery, which not only allows satellite comparisons but also removes sensor-specific characteristics and biases. Next, we empirically examine how L1b radiance calibration impacts segmentation performance. In the supplementary materials of this article, we provide the average accuracy, along with other performance metrics, for the models trained on raw sensor data. This supplementary information is provided to facilitate comparisons with the models trained on L1b radiance, as presented in Table II, in support of the upcoming analysis. To begin, for the highest-performing DL models in terms of average accuracy shown in Table III (1D-CNNs), the models exhibit slight superior performance with L1b radiance compared to training them with raw data. A similar trend occurs for the 2D models ranked just below the 1D models, which also demonstrate enhanced performance with radiance data versus raw data. Conversely, the models at the lower end of the accuracy ranking tend to perform better with raw data than radiance calibration. Concentrating only on the superior models in Table III, which hold more significance as they are the top performers, we conclude that L1b radiance calibration tends to positively impact and improve segmentation performance. We attribute the improvement to the correction of errors and biases during L1b radiance calibration, allowing top-performing

models to focus on inherent data patterns rather than overfitting on sensor-induced characteristics, leading to improved generalization performance. Nonetheless, we strongly recommend conducting comparative testing on both calibrated and raw sensor data when training the models on datasets distinct from this paper to verify whether calibrated data, such as radiance or reflectance, continues to enhance model performance.

4.1.3. Segmentation Performance (III): False Detection Ratios, Data Loss, and Downlink Inefficiency

For a more in-depth assessment of the segmentation performance for each individual class, we scrutinize which models are positioned in the lower-left corner in the scatter plots in Figs. 3, 4, and 5. The lower-left region ensures the most optimal false detection ratios, and for the example ranking system in Fig. 2, the region achieves minimal loss (or degradation) of valuable data, while also minimizing the inefficient utilization of the satellite downlink. As previously explained, lower data loss (in the Y-axis) takes precedence, while the downlink inefficiency (in the X-axis) is of lower priority since it does not result in any loss of valuable data. However, as discussed in Section 2.4, we also aim for a reasonably balanced relationship between false positives and false negatives to prevent scenarios where a model achieves a convenient minimal data loss, at the expense of extremely deteriorating the downlink efficiency. Next, we comparatively analyze the top-performing models located in the lower-left corners of Figs. 3-5.

First, we assess the models only in terms of data loss. In Fig. 3 for cloud segmentation, models such as the 2D-Justo-UNet-Simple excels in minimizing the loss of data, approaching nearly no data loss (ideal case). This signifies that the 2D-Justo-UNet-Simple outperforms by not misclassifying valuable non-cloud data (sea or land) as clouds, even if it means some cloudy data remains undetected, thus reducing the downlink efficiency. With respect to sea segmentation (Fig. 4), the 2D-UNet-FAUBAI-reduced stands out for its minimal loss of sea pixels with FNR=0.01, i.e., there is only a 1% proportion of sea pixels that remain undetected, resulting in their loss. This outperforms other models such as the 1D-Justo-LiuNet with 5% loss. Finally, in Fig. 5 for land segmentation, we observe a remarkable similarity in false alarm ratios in the lower-left optimal region, resulting in a slight overlap. Therefore, we next clarify that the optimal models, when sorted in ascending order of FNR (data loss), are as follows: 0.02 (2D-Justo-UNet-Simple), 0.03 (1D-Justo-LiuNet), 0.04 (1D-Justo-HuNet), and 0.06 (2D-CUNet++ Reduced). Consequently, the 2D-Justo-UNet-Simple is the most opti-

mal at minimizing the loss of land data, achieving only a 2% ratio of undetected land pixels.

Second, to jointly maintain a reasonable downlink efficiency while achieving low data loss, we study the models taking into account not only the data loss as in the previous analysis, but also the trade-off between both loss of data and downlink efficiency objectives. We could consider the use of Pareto fronts, which are typically applied in multi-objective optimization to address trade-offs between inversely proportional variables. Nevertheless, for simplicity, we analyze the trade-off using the Euclidean distance metric that gives equal weight to the two objectives. Specifically, we calculate the distance of each model from the origin point, representing the ideal scenario with zero false alarms. First, for cloud segmentation (Fig. 3), the models closest to the ideal performance have (FPR, FNR) values of (0.02, 0.15) for 1D-Justo-LiuNet and (0.00, 0.17) for 2D-Justo-UNet-Simple, resulting in approximate distances of 0.151 and 0.170, respectively. In brief, 1D-Justo-LiuNet exhibits the shortest distance to the ideal model. Second, the top models for sea segmentation (Fig. 4), with (FNR, FPR) of (0.08, 0.01) for 1D-Justo-LucasCNN, (0.05, 0.02) for 1D-Justo-LiuNet, and (0.04, 0.03) for 2D-UNet-FAUBAI, have approximate distances of 0.081, 0.054, and 0.050, respectively. This suggests a marginally better performance of 2D-UNet-FAUBAI, with a difference of 0.004 in distance compared to the 1D-Justo-LiuNet. However, Table II notes that the 2D-UNet-FAUBAI has over 26 million parameters, whereas our network, 1D-Justo-LiuNet, has only 4,563 parameters, which is more suitable for on-board deployment. Considering the nearly identical performance and the large parameter difference against FAUBAI’s network, 1D-Justo-LiuNet remains the top model also for sea segmentation. Finally, for land segmentation (Fig. 5), the optimal models are of (FNR, FPR) = (0.02, 0.06) for 2D-Justo-UNet-Simple, (0.03, 0.04) for 1D-Justo-LiuNet, (0.04, 0.04) for 1D-Justo-HuNet, and (0.06, 0.04) for 2D-CUNet++ Reduced, with approximate distances of 0.063, 0.050, 0.057, and 0.072, respectively. In summary, 1D-Justo-LiuNet outperforms the other models for land segmentation.

Considering the initial analysis focused solely on data loss and the subsequent analysis regarding the trade-off between both data loss and downlink efficiency, we next provide our conclusion. On the one hand, the 2D-Justo-UNet-Simple, with approximately 7 thousand parameters, minimizes the loss of valuable data for most classes. The only exception is the sea class, where it incurs an acceptable 5% data loss in contrast to the 1% loss by 2D-UNet-FAUBAI-reduced which uses around

2 million parameters and hence the FAUBAI’s network is less suitable for on-board inference. On the other hand, when we equally consider both data loss and downlink usage efficiency, our model, 1D-Justo-LiuNet, excels in minimizing data loss, achieving low rates of 2%, 5%, and 3%, while simultaneously demonstrating relatively minimal inefficiency rates of 2%, 3%, and 15% for sea, land, and cloud classes, respectively. The findings suggest that when employing 1D-Justo-LiuNet, downlink efficiency slightly deteriorates due to an under-detection of clouds, leading to an overabundance of 15% of cloud data that would be downlinked from the satellite. We attribute the finding to the dataset’s class imbalance, where the cloud class constitutes the minority. Nevertheless, the over-detection of the majority classes sea (2%) and land (3%) pixels is smaller, thereby increasing the overall efficiency of the downlink channel.

4.1.4. Segmentation Performance (IV): Priority Rankings for Downlink

As part of the further evaluation of the models’ performance, we conduct an additional analysis of the ranking system to evaluate its effectiveness in sorting HS images, as explained next. We center our analysis on the Spearman’s coefficient (Table II) to determine which model precisely ranks the images based on the sea, land, and cloud coverage levels calculated from the segmented images. According to Tables II and III, the experimental results confirm that 1D-Justo-LiuNet and 1D-Justo-HuNet are the top performers, surpassing again the state-of-the-art models. As a matter of fact, Table II shows that 1D-Justo-LiuNet and 1D-Justo-HuNet are the only models capable of reaching the ideal Spearman’s coefficient of 1.00, indicating the perfect sorting of the images in the rankings, with no errors compared to the ground-truth ranks for sea, land, and cloud levels. This emphasizes the selection of 1D-Justo-LiuNet (or possibly 1D-Justo-HuNet) as the preferred choice for the proposed on-board ranking system.

Furthermore, the results reveal that our 2D model, 2D-Justo-UNet-Simple, although not achieving the same level of ranking performance as the 1D models, also surpass most of their fellow 2D models from the state of the art. Nonetheless, our model, 1D-Justo-LucasCNN, does not produce improved results, as it only yields the same figures to those achieved by other state-of-the-art models (1D-ML/SGD, 2D-CUNet Reduced, and 2D-UNet FAUBAI).

4.1.5. Segmentation Performance (V): Model Generalisation in Deployment Set

Aligning with the segmentation literature for satellite imagery [13], we conduct generalization tests in the unseen on-ground deployment set of 30 images, relying on expert visual inspection (similar to [13]) as this set has no ground-truth labels available. From the generalization tests, we next illustrate the segmentation results for one of the deployment images, specifically a HYPSON-1 capture taken over the Namib desert in Africa [34], as depicted in Fig. 6. Fig. 6a presents the segmentation results obtained using 1D-Justo-LiuNet. The figure includes a grayscale L1b radiance image at a wavelength of $\lambda=699.61$ nm, followed by the model’s segmented image, a confidence probability map indicating the model’s certainty for each pixel-level prediction, and summarised information regarding sea, land, and cloud coverage levels used to sort the images in the ranking system. The figure illustrates that 1D-Justo-LiuNet performs adequately, with a slightly reduced certainty in class transitions while maintaining a high level of overall certainty in its predictions. Regarding 2D-CNN models, due to the limited generalization capability observed in the deployment set for 2D-Justo-UNet-Simple (which is, however, a top-performer in the test set), we choose to conduct generalization tests on other 2D-CNN models of interest instead, such as 2D-CUNet++ Reduced, as illustrated in Fig. 6b. The figure highlights that 2D-CUNet++ Reduced encounters important misclassifications at the non-overlapping patch borders, consistent with the confidence observed in the patch edges in addition to the decreased certainty in the class transitions. This phenomenon may be attributed to a variety of factors, including the network’s padding of input patches, among other potential causes.

In the supplementary material for the generalisation tests on the rest of the deployment set, we provide the outcomes for the remaining deployment images. From the overall on-ground deployment, we conclude that 1D-Justo-LiuNet generalizes acceptably for our needs. However, its 1D-CNN architecture can result in predictions with higher entropy, leading to less smooth class transitions. This is attributed to the absence of spatial context in its pixel-level predictions. On the other hand, 2D-CUNet++ Reduced, while still generalizing effectively, exhibits higher misclassifications at patch borders. Nevertheless, it remarkably provides predictions with lower entropy, resulting in smoother class transitions, due to the utilization of spatial neighboring information during pixel-level predictions.

4.1.6. Segmentation Performance (VI): Summary

In light of the previous sections, in addition to the key finding that 1D models outperform their 2D counterparts in our experiments, we conclude that the 1D-Justo-LiuNet model consistently outperforms the current state-of-the-art models, all trained for the same sea-land-cloud segmentation task in HYPSON-1 L1b calibrated data. Specifically, the 1D-Justo-LiuNet surpasses the literature in terms of segmentation performance, assessed by average accuracy and false detection ratios trade-off. Furthermore, our results for the 1D-Justo-LiuNet not only surpass the performance reported by the soil spectroscopy literature [45], but our findings also exhibit remarkable consistency, even within the context of the ranking system application case (Spearman’s coefficient), where the 1D-Justo-LiuNet also outperforms the other models. Additionally, 1D-Justo-LiuNet demonstrates acceptable performance when subjected to generalization tests on the unseen on-ground deployment set. However, we stress that our results and conclusions are specific to the sea-land-cloud dataset [34], and we acknowledge that model performance may differ when the data source is altered in any manner. For instance, a model that performs well on one dataset may not excel on another. To facilitate testing of the models used in this work on other data sources, we provide the software code for all models in the supplementary materials accompanying this paper.

4.1.7. Parameter Count

Following the analysis of the models’ performance, we next examine the number of model parameters (Table II) that need to be uplinked to a satellite for in-orbit deployment. Our lightweight model 1D-Justo-LiuNet surpasses the existing literature in terms of parameter count ranking at the top (Table III), as the model with the fewest parameters (4,563), even when compared to other lightweight models in the literature, such as 2D-CUNet, 2D-CUNet++, 2D-CUNet Reduced, and 2D-CUNet++ Reduced. Hence, the lightweight 1D-Justo-LiuNet model stands out as the most practical choice when solely considering the reduction in on-board memory required for storing the model parameters. Moreover, despite some of our other models, such as 1D-Justo-HuNet and 2D-Justo-UNet-Simple, exhibit a slight increase in the number of parameters compared to 1D-Justo-LiuNet, they still maintain their parameter count below ten thousands, which is still lower than the number of parameters of the other state-of-the-art models. As mentioned earlier, the lowest-ranked 2D-UNet FAUBAI network utilizes over 26 million parameters. Even its reduced version, 2D-UNet FAUBAI re-

duced, has nearly 2 million parameters, which we also find excessive for on-board deployment while it does not improve the model’s performance neither in terms of segmentation accuracy nor in terms of image ranking. Finally, we emphasize that a significant majority of our top models in terms of performance (accuracy and Spearman’s coefficient in Table III), also occupy the best ranks in terms of parameter count. Therefore, we can assert that we achieve our objective outlined in Section 2 regarding surpassing the state-of-the-art performance, while significantly compressing the models.

4.1.8. Inference Time

The final metric of our analysis is the average inference time per HS image (Table II). Despite the strengths of the 1D models, with particular emphasis on the favorable results by the 1D-Justo-LiuNet, 1D models exhibit a drawback of extended inference times on the processing architecture used in the tests, even considering their low parameter count. In Table II, we observe that both 1D ML and DL models, especially DL models with more intrinsic complexity, exhibit lengthier inference times. In fact, the results reveal that the 1D-Justo-LiuNet has the lengthiest inference time, at around 15 seconds for a single HS image. The results demonstrate, however, that 2D models significantly decrease the inference time, reducing it to the order of milliseconds. The disparity in speed may be attributed due to the potentially greater number of floating-point operations per second (FLOPS) required by the 1D models, among other factors affecting the inference time.

Although satellites like HYPSON-1 experience data latency lasting minutes to hours [29], we propose the following solution if inference times in the order of seconds (e.g., by 1D-Justo-LiuNet) are perceived as lengthy for in-orbit inference. Employing the HYPSON-1 satellite as an example case, its On-board Processing Unit (OPU) integrates an FPGA System-on-Chip (Zynq-7030/XC7Z030-1) [10]. The system features an ARM Cortex-A9 processor and provides superior FPGA logic resources in comparison to other platforms, such as the Zynq-7020, previously employed in cloud detection within satellite imagery [14]. As future work, we suggest implementing the 1D-Justo-LiuNet in the processor side to confirm whether the inference time is still lengthy. We anticipate that the processor’s lower-level software implementation may yield shorter inference times compared to running inference in higher-level languages like Python. If the inference time would still remain too long, we recommend a combined software-hardware co-design approach. This approach accelerates computationally intensive tasks for faster in-

ference, while maintaining low power consumption, by using the FPGA fabric logic.

4.2. Results Analysis for Models Trained on 3 Channels

We finalize the discussion section by addressing the impact of reducing the number of channels from 112 to 3 on the reported metrics. As indicated in Table IV, when we train the models using the 3-channel dataset instead, the inference times decrease compared to the models trained with 112 channels, as there is now less data to process. Moreover, there is a reduction in the number of model parameters due to the smaller number of components within each convolutional kernel when computing the respective 2D convolutions across the reduced spectral dimension. Nevertheless, the reduction in feature channels leads to a decreased segmentation performance, with the highest accuracy reaching 0.87, unlike the 0.93 top accuracy for the models trained with 112 channels. The decline in performance is also evident in the evaluation of the ranking system, for which none of the models achieve the ideal coefficient of 1.00, as observed earlier with 112 channels. As a matter of fact, the highest Spearman’s coefficient for 3 channels is notably lower at 0.83.

5. Conclusion

In this work, we conducted experiments including the training and comparison of 16 machine learning and deep learning models, whose software codes are provided within this article along with additional supplementary materials, for future in-orbit deployment using the Sea-Land-Cloud-Labeled dataset from the HYPSON-1 mission [34], as an illustrative case. Our experiments demonstrated that when segmenting sea, land, and cloud categories in hyperspectral satellite imagery, 1D models surpass 2D models in terms of performance. This conclusion also holds for our proposed ranking system combining priority downlink according to sea, land and cloud coverage. Our proposed lightweight models, such as 1D-Justo-LiuNet and 1D-Justo-HuNet, consistently surpass the performance of state-of-the-art models. Moreover, they demonstrate remarkable model compression, reaching up to 90.50% when compared to the existing models. This makes 1D-Justo-LiuNet and 1D-Justo-HuNet well-suited for future in-flight deployment. Furthermore, we also found that using L1b calibrated radiance data, instead of raw sensor data, improved segmentation performance. Moreover, training models with only three spectral channels led to shorter inference times and reduced parameter counts, at the cost of lower segmentation performance. Finally, as future work, we suggest to study the implementation

of processing architectures that are used aboard satellites and conducting experimental tests to deploy, for instance, the 1D-Justo-LiuNet model in orbit.

Declaration of Competing Interest

The authors declare that they have no known competing interests that could have appeared to influence the work reported in this paper.

Data availability

To begin, the labeled dataset used in this paper is openly available to download at https://ntnu-smallsat-lab.github.io/hypso1_sea_land_clouds_dataset/. Our supplementary material is openly available at https://github.com/NTNU-SmallSat-Lab/s_l_c_segm_hyp_img/. We provide the following resources. Firstly, the Python model codes accompanied by a notebook that illustrates how to perform inference on HYPISO-1 data, by 1D-CNN and 2D-CNN models. Secondly, there is an executable software program designed to serve as an oceanic-terrestrial-cloud segmenter for hyperspectral imagery acquired by the HYPISO-1 satellite. Thirdly, we provide trained models with learned parameters, with 46 distinct configurations, for the HYPISO-1 data. Fourth, we offer additional in-depth architectural details for the models. Fifth, we include information regarding the training, validation, and test data splits. Sixth, we share an extensive set of experimental figures, including multiple metrics. Seventh, we provide a deployment set consisting of 30 unlabeled HYPISO-1 images. Lastly, we present the generalisation tests in the complete deployment set.

Acknowledgements

The research leading to these results has received funding from the NO Grants 2014 – 2021, under Project ELO-Hyp contract no. 24/2020, and the Research Council of Norway grant no. 328724 (Green Platform) and no. 325961 (HYPSCI). We extend our gratitude to Anum Masood, Per Gunnar Kjeldsberg, and Simen Neteland.

Appendix A. Direct Channel Reduction

Considering that the legacy algorithms for cloud detection in HS satellite imagery typically select 3 channels to mimic RGB image processing [11–14], we also obtain another dataset by reducing the 112 channels to

merely 3 channels. To achieve this reduction, we explore the literature of dimensionality reduction extensively studied for HS satellite missions [46–48]. First, the focus on reducing dimensions originates from the importance of having low-dimensional data which can save computation resources, memory usage and power. Next, some of the techniques proposed by the literature include methods like Principal Component Analysis (PCA) [49] and Independent Component Analysis (ICA) [50]. In alignment with the state-of-the-art techniques, we employ PCA to reduce the 112 channels (normalized) to 3. To alleviate to a certain extent the computational demands of satellites operating often with tight power constraints, we propose to conduct both the training and inference of PCA exclusively on the ground. Eliminating PCA inference on the satellite enables potential power savings, which could be of importance to conduct the subsequent segmentation inference during flight. Consequently, and as also outlined by the literature [12], we suggest implementing on board a direct channel selection (3 channels) instead of deploying PCA inference. In this work, the purpose of employing PCA only on ground is to identify in advance the channels containing the most useful information in the data. In particular, we use PCA to identify the channels that have the greatest influence on a single principal component, as determined by the weight loadings of those channels. In the case of the 112-channel L1b dataset, we find that the majority of influential channels are predominantly within the NIR range. However, given the necessity of considering other spectral ranges in addition to NIR for the adequate segmentation of sea, land, and clouds – as the NIR range alone is likely to be insufficient – we opt to pick the top three influential channels from only the visible blue, second the visible green and red combined, and finally the NIR. In the dataset, the most influential channels within each spectral range are: 412.72 nm (channel 7) for the blue spectrum, 699.61 nm (channel 89) in the green and red spectra, and 747.77 nm (channel 103) in the NIR spectrum. These align closely with the L1b radiance bands frequently analyzed during HYPISO-1 operations, especially for channels 89 and 103.

Appendix B. Data Dimensions Arrangement

On the one hand, in the case of 1D-CNN or 1D ML models, we transform each HS image into a 2D array resembling tabular data. Therefore, the models take inputs formatted as $BATCH\ SIZE \times CHANNELS$, where $BATCH\ SIZE$ indicates the number of image pixels for

which predictions are to be inferred. 1D-CNN models perform 1D convolutions separately on each pixel across its channels. On the other hand, for 2D-CNNs, optimizing memory and computational resources during training and inference is even more essential, and to help achieving this, we divide each HS image datacube into smaller cubes, often referred as 3D patches or tiles. Padding extends the image borders to retain the integrity of edge information, and the padded borders can be eliminated by cropping the extended spatial dimensions in the segmented image. After padding, we proceed with non-overlapping patching. Unlike overlapping patching, this approach guarantees that each pixel is processed only once to reduce computational complexity. The input format for the 2D-CNNs is $BATCH\ SIZE \times PATCH\ SIZE \times PATCH\ SIZE \times CHANNELS$, where $BATCH\ SIZE$ refers in this case to the number of 3D patches. We find that a $PATCH\ SIZE$ of 48 is suitable for our experiments as it aligns with the encoder-decoder networks, which repeatedly decrease the spatial dimensions by a factor of two via pooling. Consequently, selecting a $PATCH\ SIZE$ of 48 ensures that the spatial dimensions subjected to pooling remain integer as the network's depth increases while reducing memory and computational resources in forward propagation.

References

- [1] M. Esposito, S. S. Conticello, M. Pastena, B. C. Domínguez, In-orbit demonstration of artificial intelligence applied to hyperspectral and thermal sensing from space, in: *CubeSats and SmallSats for remote sensing III*, Vol. 11131, SPIE, 2019, pp. 88–96.
- [2] S. Cogliati, F. Sarti, L. Chiarantini, M. Cosi, R. Lorusso, E. Lopinto, F. Miglietta, L. Genesio, L. Guanter, A. Damm, et al., The prisma imaging spectroscopy mission: Overview and first performance analysis, *Remote sensing of environment* 262 (2021) 112499.
- [3] M. Cosmo, F. Battazza, F. Caltagirone, F. Covelto, G. De Luca, R. Formaro, F. Longo, G. Varacalli, The future eo asi missions are based on sar and hyperspectral sensors, in: *IAC-12-B1. 2.8, 63rd International Astronautical Congress*, 2014.
- [4] L. Guanter, H. Kaufmann, K. Segl, S. Foerster, C. Rogass, S. Chabrilat, T. Kuester, A. Hollstein, G. Rossner, C. Chlebek, et al., The enmap spaceborne imaging spectroscopy mission for earth observation, *Remote Sensing* 7 (7) (2015) 8830–8857.
- [5] M. E. Grøtte, R. Birkeland, E. Honoré-Livermore, S. Bakken, J. L. Garrett, E. F. Prentice, F. Sigernes, M. Orlandić, J. T. Grasdahl, T. A. Johansen, Ocean color hyperspectral remote sensing with high resolution and low latency—the hypso-1 cubesat mission, *IEEE Transactions on Geoscience and Remote Sensing* 60 (2021) 1–19.
- [6] J. Nieke, M. Rast, Towards the copernicus hyperspectral imaging mission for the environment (chime), in: *Igarss 2018-2018 ieee international geoscience and remote sensing symposium*, IEEE, 2018, pp. 157–159.
- [7] J. Nieke, L. Despoisse, A. Gabriele, H. Weber, H. Strese, N. Ghasemi, F. Gascon, K. Alonso, V. Boccia, B. Tsonevska, et al., The copernicus hyperspectral imaging mission for the environment (chime): an overview of its mission, system and planning status, *Sensors, Systems, and Next-Generation Satellites XXVII 12729* (2023) 21–40.
- [8] H. M. Dierssen, M. Gierach, L. S. Guild, A. Mannino, J. Salisbury, S. S. Uz, J. Scott, P. A. Townsend, K. Turpie, M. Tzortziou, E. Urqihart, R. Vandermeulen, P. J. Werdell, Synergies between NASA's hyperspectral aquatic missions PACE, GLIMR, and SBG: Opportunities for new science and applications, *Journal of Geophysical Research: Biogeosciences* 128 (2023) e2023JG007574.
- [9] L. ANSALE, The prisma and prisma-psg missions status and updates (2022).
- [10] D. D. Langer, M. Orlandić, S. Bakken, R. Birkeland, J. L. Garrett, T. A. Johansen, A. J. Sørensen, Robust and reconfigurable on-board processing for a hyperspectral imaging small satellite, *Remote Sensing* 15 (15) (2023) 3756.
- [11] G. Giuffrida, L. Diana, F. de Gioia, G. Benelli, G. Meoni, M. Donati, L. Fanucci, Cloudscout: A deep neural network for on-board cloud detection on hyperspectral images, *Remote Sensing* 12 (14) (2020) 2205.
- [12] G. Giuffrida, L. Fanucci, G. Meoni, M. Batič, L. Buckley, A. Dunne, C. van Dijk, M. Esposito, J. Hefele, N. Vercruyssen, et al., The ϕ -sat-1 mission: The first on-board deep neural network demonstrator for satellite earth observation, *IEEE Transactions on Geoscience and Remote Sensing* 60 (2021) 1–14.
- [13] C. Salazar, J. Gonzalez-Llorente, L. Cardenas, J. Mendez, S. Rincon, J. Rodriguez-Ferreira, I. F. Acero, Cloud detection autonomous system based on machine learning and cots components on-board small satellites, *Remote Sensing* 14 (21) (2022) 5597.
- [14] R. Pitonak, J. Mucha, L. Dobis, M. Javorka, M. Marusin, Cloudsatnet-1: Fpga-based hardware-accelerated quantized cnn for satellite on-board cloud coverage classification, *Remote Sensing* 14 (13) (2022) 3180.
- [15] D. Spiller, K. Thangavel, S. T. Sasidharan, S. Amici, L. Ansalone, R. Sabatini, Wildfire segmentation analysis from edge computing for on-board real-time alerts using hyperspectral imagery, in: *2022 IEEE International Conference on Metrology for Extended Reality, Artificial Intelligence and Neural Engineering (MetroXRaine)*, IEEE, 2022, pp. 725–730.
- [16] D. Lebedeff, M. F. Foulon, R. Camarero, R. Vitulli, Y. Bobichon, On-board cloud detection and selective spatial/spectral compression based on ccstds 123.0-b-2 for hyperspectral missions, in: *7th ESA International Workshop on On-Board Payload Data Compression Conference (OBPDC)*, 2020.
- [17] J. Gjendem Røysland, Real-time classification onboard the hypso-1 satellite, Master's thesis, NTNU (2023).
- [18] J. Røysland, D. Langer, S. Berg, M. Orlandić, J. Garrett, Hyperspectral classification onboard the hypso-1 cubesat, in: *WHISPERS*, 2023.
- [19] V. Kothari, E. Liberis, N. D. Lane, The final frontier: Deep learning in space, in: *Proceedings of the 21st international workshop on mobile computing systems and applications*, 2020, pp. 45–49.
- [20] C. Giovanni, B. Eliot, Technology transfer and capability building for Colombia's space program by means of small satellites, in: *Proceedings of the International Astronautical Congress, IAC*, Vol. 2019-October, 2019.
- [21] M. Hernández-Cabronero, A. B. Kiely, M. Klimesh, I. Blanes, J. Ligo, E. Magli, J. Serra-Sagrasta, The ccstds 123.0-b-2 “low-complexity lossless and near-lossless multispectral and hyperspectral image compression” standard: A comprehensive review, *IEEE Geoscience and Remote Sensing Magazine* 9 (4) (2021) 102–119.

- [22] R. Birkeland, S. Berg, M. Orlandic, J. Garrett, On-board characterization of hyperspectral image exposure and cloud coverage by compression ratio, in: *2022 12th Workshop on Hyperspectral Imaging and Signal Processing: Evolution in Remote Sensing (WHISPERS)*, IEEE, 2022, pp. 1–5.
- [23] J. A. Justo, D. Lupu, M. Orlandić, I. Necoara, T. A. Johansen, A comparative study of compressive sensing algorithms for hyperspectral imaging reconstruction, in: *2022 IEEE 14th Image, Video, and Multidimensional Signal Processing Workshop (IVMSP)*, IEEE, 2022, pp. 1–5.
- [24] J. A. Justo, M. Orlandić, Study of the gomp algorithm for recovery of compressed sensed hyperspectral images, in: *2022 12th Workshop on Hyperspectral Imaging and Signal Processing: Evolution in Remote Sensing (WHISPERS)*, IEEE, 2022, pp. 1–5.
- [25] G. Furano, G. Meoni, A. Dunne, D. Moloney, V. Ferlet-Cavrois, A. Tavoularis, J. Byrne, L. Buckley, M. Psarakis, K.-O. Voss, et al., Towards the use of artificial intelligence on the edge in space systems: Challenges and opportunities, *IEEE Aerospace and Electronic Systems Magazine* 35 (12) (2020) 44–56.
- [26] Y. Wang, J. Yang, X. Guo, Z. Qu, Satellite edge computing for the internet of things in aerospace, *Sensors* 19 (20) (2019) 4375.
- [27] A. Raoofy, G. Dax, V. Serra, M. Ghiglione, M. Werner, C. Trinitis, Benchmarking and feasibility aspects of machine learning in space systems, in: *Proceedings of the 19th ACM International Conference on Computing Frontiers*, 2022, pp. 225–226.
- [28] M. Ghiglione, A. Raoofy, G. Dax, G. Furano, R. Wiest, C. Trinitis, M. Werner, M. Schulz, M. Langer, Machine learning application benchmark for in-orbit on-board data processing, in: *European Workshop on On-Board Data Processing*, 2021.
- [29] S. Bakken, M. B. Henriksen, R. Birkeland, D. D. Langer, A. E. Oudijk, S. Berg, Y. Pursley, J. L. Garrett, F. Gran-Jansen, E. Honoré-Livermore, M. E. Grøtte, B. A. Kristiansen, M. Orlandic, P. Gader, A. J. Sørensen, F. Sigernes, G. Johnsen, T. A. Johansen, HYPSON-1 CubeSat: First Images and In-Orbit Characterization, *Remote Sensing* 15 (3) (2023) 755.
- [30] A. Dallolio, G. Quintana-Diaz, E. Honoré-Livermore, J. L. Garrett, R. Birkeland, T. A. Johansen, A satellite-usv system for persistent observation of mesoscale oceanographic phenomena, *Remote Sensing* 13 (16) (2021) 3229.
- [31] G. Furano, A. Menicucci, Roadmap for on-board processing and data handling systems in space, *Dependable Multicore Architectures at Nanoscale* (2018) 253–281.
- [32] M. Antonini, T. H. Vu, C. Min, A. Montanari, A. Mathur, F. Kawsar, Resource characterisation of personal-scale sensing models on edge accelerators, in: *Proceedings of the First International Workshop on Challenges in Artificial Intelligence and Machine Learning for Internet of Things*, 2019, pp. 49–55.
- [33] W. Li, M. Liewig, A survey of ai accelerators for edge environment, in: *Trends and Innovations in Information Systems and Technologies: Volume 2* 8, Springer, 2020, pp. 35–44.
- [34] J. A. Justo, J. Garrett, D. D. Langer, M. B. Henriksen, R. T. Ionescu, T. A. Johansen, An open hyperspectral dataset with sea-land-cloud ground-truth from the hypso-1 satellite, *arXiv preprint arXiv:2308.13679* (2023, Accepted).
- [35] M. B. Henriksen, E. F. Prentice, T. A. Johansen, F. Sigernes, Pre-launch calibration of the hypso-1 cubesat hyperspectral imager, in: *2022 IEEE Aerospace Conference (AERO)*, IEEE, 2022, pp. 1–9.
- [36] D. Wark, D. Mercer, Absorption in the atmosphere by the oxygen “a” band, *Applied Optics* 4 (7) (1965) 839–845.
- [37] L. Bouter, B. van Diedenhoven, Satellite remote sensing of cloud properties in support of tropospheric trace gas retrievals (2007).
- [38] J. H. Park, T. Inamori, R. Hamaguchi, K. Otsuki, J. E. Kim, K. Yamaoka, Rgb image prioritization using convolutional neural network on a microprocessor for nanosatellites, *Remote Sensing* 12 (23) (2020) 3941.
- [39] G. Bahl, L. Daniel, M. Moretti, F. Lafarge, Low-power neural networks for semantic segmentation of satellite images, in: *Proceedings of the IEEE/CVF International Conference on Computer Vision Workshops*, 2019, pp. 0–0.
- [40] O. Ronneberger, P. Fischer, T. Brox, U-net: Convolutional networks for biomedical image segmentation, in: *Medical Image Computing and Computer-Assisted Intervention–MICCAI 2015: 18th International Conference, Munich, Germany, October 5–9, 2015, Proceedings, Part III* 18, Springer, 2015, pp. 234–241.
- [41] S. Tagestad, Hardware acceleration of a compact cnn model for semantic segmentation of hyperspectral satellite images, Master’s thesis, Norwegian University of Science and Technology (2021).
- [42] S. Nettelund, Exploration and implementation of large cnn models for image segmentation in hyperspectral cubesat missions, Master’s thesis, Norwegian University of Science and Technology (2022).
- [43] L. Liu, M. Ji, M. Buchroithner, Transfer learning for soil spectroscopy based on convolutional neural networks and its application in soil clay content mapping using hyperspectral imagery, *Sensors* 18 (9) (2018) 3169.
- [44] W. Hu, Y. Huang, L. Wei, F. Zhang, H. Li, Deep convolutional neural networks for hyperspectral image classification, *Journal of Sensors* 2015 (2015) 1–12.
- [45] F. M. Riese, S. Keller, Soil texture classification with 1d convolutional neural networks based on hyperspectral data, *arXiv preprint arXiv:1901.04846* (2019).
- [46] S. Bakken, M. Orlandic, T. A. Johansen, The effect of dimensionality reduction on signature-based target detection for hyperspectral remote sensing, in: *CubeSats and SmallSats for remote sensing III*, Vol. 11131, SPIE, 2019, pp. 164–182.
- [47] S. Bakken, Development of a small satellite with a hyperspectral imaging payload and onboard processing for ocean color, Ph.D. thesis, Norwegian University of Science and Technology (2022).
- [48] C. Penne, J. Garrett, T. Johansen, M. Orlandic, R. Heggebø, G. Seafood, Independent component analysis: A tool for algal bloom detection.
- [49] C. Rodarmel, J. Shan, Principal component analysis for hyperspectral image classification, *Surveying and Land Information Science* 62 (2) (2002) 115–122.
- [50] D. Lupu, I. Necoara, J. L. Garrett, T. A. Johansen, Stochastic higher-order independent component analysis for hyperspectral dimensionality reduction, *IEEE Transactions on Computational Imaging* 8 (2022) 1184–1194.